UCRL-ID-147761

Direct Numerical Simulation of a Shocked Helium Jet

L. D. Cloutman

February 1, 2002

U.S. Department of Energy
Lawrence Livermore National Laboratory

DISCLAIMER

This work was performed under the auspices of the U. S. Department of Energy by the University of California, Lawrence Livermore National Laboratory under Contract No. W-7405-Eng-48.

Lawrence Livermore National Laboratory report
UCRL-ID-??????
February 2002

DIRECT NUMERICAL SIMULATION OF A SHOCKED HELIUM JET

Lawrence D. Cloutman

Abstract

We present direct numerical simulations of a shock tube experiment in which a cylindrical laminar jet of helium doped with biacetyl is injected into air and subjected to a weak shock wave. Computed species distributions in a planar cross section of the jet are compared to planar laser-induced fluorescence (PLIF) images produced by the experiment. The calculations are in excellent agreement with the experimental images. We find that differential diffusion of species is an important feature of this experiment.

1 Introduction

Turbulent mixing plays a fundamental role in a wide variety of applications, yet the details of how chemical inhomogeneities get damped or even eliminated are not well understood. One approach to gaining insight into this process is to study highly simplified and idealized situations that are amenable to detailed experimental and numerical studies. One such experiment involves subjecting laminar cylindrical jets of helium and sulfur hexafluoride in air to weak shock waves in a shock tube [1, 2, 3] and watching the distortion and breakup of the jets. This report describes a prelimiary direct numerical simulation (DNS) of the helium-jet case using the COYOTE computational fluid dynamics program [4].

In a companion report [5], similar simulations were reported for a 24 μm sphere of xenon immersed in helium at a temperature of 2000 K. The combination of small size and high temperature causes diffusion to rapidly mix the two gases at the atomic level, which leads to very simple structures even when the sphere is shocked. The present experiment is conducted at a lower temperature and at a larger length scale, which implies a higher Reynolds number, so considerably more structure is seen in the species concentration plots.

The geometry of the experiment is quite simple. A horizontal shock tube is fitted with the appropriate plumbing to produce a vertical laminar jet in the test section, which is 26.67 cm square. The jet inflow can be on either the bottom or top of the shock tube, so buoyancy forces can be used to help stabilize the jet. On the opposite wall, there is a larger opening that is used to exhaust the jet so the jet material does not accumulate inside the shock tube. In the case of a helium jet, the flow is upwards. For sulfur hexafluoride, which is denser than air, the jet flows downward. Once a stable cylindrical jet is produced, a planar shock wave is produced that impacts the jet on the upstream side of the cylinder. The transit time of the shock across the diameter of the cylinder is much smaller than the transit time of the gas jet across the width of the shock tube, so one effect of the shock passage is to tear a cylinder of gas away from the jet and start it moving downstream along with the post-shock air stream. In addition, there is a complex flow set up within the cylinder by the shock passage. Initially there is a one-dimensional compression of the cylinder, changing its cross section from circular to elliptical. In addition, baroclinic torques produce vorticity at

the edge of the cylinder, inducing flow that turns the elliptical cross section into a vortex pair with a complex internal structure. This internal structure and its evolution are the main topic of this report.

The experimental results are in the form of a time sequence of planar laser-induced fluorescence (PLIF) images. The fluorescence is produced by a small amount of biacetyl (2,3-butanedione, $CH_3COCOCH_3$) mixed with the jet gas. The image plane is horizontal and either 2.54 or 3.81 cm above the jet orifice, depending on which experiment is being considered. The simulations are two-dimensional in Cartesian coordinates and solve the Navier-Stokes equations with a detailed treatment of molecular transport. The grid lies in the PLIF image plane. This should be a good approximation since this is basically a laminar flow with little variation along the length of the jet/cylinder.

Section 2 summarizes the governing equations. Section 3 presents numerical solutions. Conclusions are presented in Section 4.

2 Governing Equations

The simulations were performed with the COYOTE computational fluid dynamics program [4], which is based on the full transient multicomponent Navier-Stokes equations. The model includes a real-gas caloric equation of state, arbitrary chemical kinetics, transport coefficients from a Lennard-Jones model, a simple radiative heat loss model, and mass diffusion based on the full Stefan-Maxwell equations. Chemistry and radiation are omitted from the present calculations.

Mass conservation is expressed by the continuity equation for each species α:

$$\frac{\partial \rho_\alpha}{\partial t} + \nabla \cdot (\rho_\alpha \mathbf{u}) = -\nabla \cdot \mathbf{J}_\alpha + R_\alpha, \tag{1}$$

where ρ_α is the density of species α, $\mathbf{u}$ is the fluid velocity, $\mathbf{J}_\alpha$ is the diffusional mass flux of species α, and R_α is the rate of change of species α by chemical reactions. The diffusional flux is a complex function of the flow that will be described shortly. The total density ρ is obtained by summing the ρ_α.

The momentum equation is

$$\frac{\partial(\rho \mathbf{u})}{\partial t} + \nabla \cdot (\rho \mathbf{u}\mathbf{u}) = \sum_{\alpha} \rho_{\alpha} \mathbf{F}_{\alpha} - \nabla P + \nabla \cdot \mathsf{S}, \tag{2}$$

where P is the pressure, and $\mathbf{F}_{\alpha}$ is the body force per unit mass acting on species α, which in most applications is the gravitational acceleration $\mathbf{g}$. We assume that the viscous stress tensor is

$$\begin{aligned} \mathsf{S} &= \mu \left[\nabla \mathbf{u} + (\nabla \mathbf{u})^{\mathrm{T}}\right] + \mu_1 (\nabla \cdot \mathbf{u})\, \mathsf{U} \\ &= \mu \left[\nabla \mathbf{u} + (\nabla \mathbf{u})^{\mathrm{T}}\right] + \left(\mu_b - \frac{2\mu}{3}\right) (\nabla \cdot \mathbf{u})\, \mathsf{U}, \end{aligned} \tag{3}$$

where μ is the coefficient of viscosity, μ_1 is the second coefficient of viscosity, U is the unit tensor, and μ_b is the bulk viscosity. In almost all studies, the bulk viscosity is set to zero, which is correct, strictly speaking, only for perfect monatomic gases.

We choose the thermal internal energy equation to express energy conservation:

$$\frac{\partial(\rho I)}{\partial t} + \nabla \cdot (\rho I \mathbf{u}) = -P \nabla \cdot \mathbf{u} + \mathsf{S} : \nabla \mathbf{u} - \nabla \cdot \mathbf{q} + \sum_{\alpha} H_{\alpha} R_{\alpha} + \sum_{\alpha} \mathbf{F}_{\alpha} \cdot \mathbf{J}_{\alpha}, \tag{4}$$

where I is the specific thermal internal energy, $\mathbf{q}$ is the heat flux, and H_{α} is the heat of formation of species α. Note that for $\mathbf{F}_{\alpha} = \mathbf{g}$, the last term vanishes.

Closing these equations for a multicomponent fluid requires specifying mass and heat fluxes, plus several transport coefficients. This topic is quite complex, and we shall limit our present discussion to an approximate closure that has been used for combustion applications. It is applicable to dilute, unionized gases for which Chapman-Enskog theory is a good approximation. That is, the molecular distribution functions have only small departures from Maxwellian and gradient lengths are much greater than the mean free path. The heat flux $\mathbf{q}$ used in COYOTE is [6, 7]

$$\mathbf{q} = -K \nabla T + \sum_{\alpha} h_{\alpha}(T) \mathbf{J}_{\alpha} - \sum_{\alpha} \frac{RT}{M_{\alpha} X_{\alpha}} D_{\alpha}^{T} \mathbf{d}_{\alpha}, \tag{5}$$

where R is the gas constant, M_{α} is the species molecular weight, X_{α} is the species mole fraction, T is the temperature, K is the multicomponent thermal conductivity, h_{α} is the specific enthalpy of species α, D_{α}^{T} is the multicomponent thermal diffusion coefficient, and

$$\mathbf{d}_{\alpha} = \nabla X_{\alpha} + (X_{\alpha} - Y_{\alpha}) \frac{\nabla P}{P} - \frac{1}{P} \left[\rho_{\alpha} \mathbf{F}_{\alpha} - Y_{\alpha} \sum_{\beta} \rho_{\beta} \mathbf{F}_{\beta}\right], \tag{6}$$

where Y_α is the species mass fraction ρ_α/ρ.

The thermal equation of state is assumed to be given as the sum of the partial pressures of an ideal gas for each species. The caloric equation of state is given as the species-density-weighted sum of the species thermal internal energies, each of which is a function only of temperature. The JANAF tables [8, 9, 10] provide a homogeneous set of thermochemical data for a large collection of materials, and these tables are used to supply the specific enthalpy and heat of formation for each species of interest. These enthalpies are easily converted into internal energies.

In the present study, we use the Lennard-Jones model to estimate the transport coefficients [11]. This model provides a viscosity (in cgs units; to get SI units, multiply the cgs viscosity by 0.1) for each species,

$$\mu_\alpha \;=\; \frac{5}{16}\left(\frac{m_{\rm H}k_{\rm B}}{\pi}\right)^{1/2}\frac{(M_\alpha T)^{1/2}}{\sigma_\alpha^2\Omega_\nu} \;=\; 2.6693\times10^{-5}\frac{(M_\alpha T)^{1/2}}{\sigma_\alpha^2\Omega_\nu}, \tag{7}$$

where $m_{\rm H}$ is the mass of one atomic mass unit in grams, $k_{\rm B}$ is the Boltzmann constant, σ_α is the collision diameter in Å, and Ω_ν is the collision integral approximated by

$$\Omega_\nu \;=\; 1.147\,(T/T_{e\alpha})^{-0.145} \;+\; (T/T_{e\alpha}+0.5)^{-2}, \tag{8}$$

where $T/T_{e\alpha} \;=\; T\,k_{\rm B}/\epsilon_\alpha$ is the reduced temperature and ϵ_α is the Lennard-Jones potential well depth [12, 13]. Kee, *et al.* [6] recommend interpolation in Table V of Monchick and Mason [14], which includes dependence of the collision integral on the reduced dipole moment of the molecule, δ, as well as dependence on $T_{e\alpha}$. Equation 8 is accurate to a few percent for Monchick and Mason's $\delta < 0.5$ at low temperatures, and it becomes more accurate for larger values of δ at higher temperatures. Table 1 lists some properties, including the Lennard-Jones parameters, for the gases used in this study.

Once the species viscosities have been calculated, they must be combined to provide the viscosity of the fluid mixture. We adopt Wilke's law [15, 16]. For N species,

$$\mu = \sum_{\alpha=1}^{N}\frac{X_\alpha\mu_\alpha}{\sum_{\beta=1}^{N}X_\beta\Phi_{\alpha\beta}}, \tag{9}$$

where

$$\Phi_{\alpha\beta} \;=\; 8^{-1/2}\left(1+\frac{M_\alpha}{M_\beta}\right)^{-1/2}\left[1+\left(\frac{\mu_\alpha}{\mu_\beta}\right)^{1/2}\left(\frac{M_\beta}{M_\alpha}\right)^{1/4}\right]^2. \tag{10}$$

Table 1. Gas Properties

No.	Species	M_α	σ_α	ϵ/k
1	C_6H_{14}	8.61783600D+01	5.909D+00	4.130D+02
2	O_2	3.19988000D+01	3.458D+00	1.074D+02
3	N_2	2.80134000D+01	3.621D+00	9.753D+01
4	CO_2	4.40100000D+01	3.763D+00	2.440D+02
5	H_2O	1.80152800D+01	2.641D+00	8.091D+02
6	Ar	3.99480000D+01	3.330D+00	1.365D+02
7	He	4.00260000D+00	2.576D+00	1.020D+01
8	SF_6	1.46050418D+02	5.252D+00	2.077D+02

In the original COYOTE program, K was calculated from the mixture viscosity μ and a constant mixture Prandtl number. This capability has been expanded to allow calculation of the conductivity based on the local composition and temperature, just as was done for the viscosity. Following the procedure of Hayashi and Hishida [12], we calculate the conductivity from the viscosity using the Eucken correction, which is discussed also by Ferziger and Kaper [17] and by Hirschfelder, Curtiss, and Bird [7]:

$$K_\alpha \;=\; 0.25\,(9\gamma_\alpha - 5)\mu_\alpha\, C_{\mathrm{v}\alpha}, \tag{11}$$

where $C_{\mathrm{v}\alpha}$ is the specific heat at constant volume and γ_α is the ratio of specific heats. Kee, *et al.* [6] describe a more complex approximation that we have not implemented. Their model accounts more accurately for the internal quantum states of the molecules.

We do not use the true multicomponent thermal conductivity, but an approximation called the "mixture averaged model" in the CHEMKIN program [6]. There are two possible mixture rules for the conductivity. The first is to use Eq. 9 with μ_α replaced by K_α, but with the same values of $\Phi_{\alpha\beta}$ as used for the mixture viscosity [16]. The second rule is due to Mathur *et al.* [18] and is recommended by Kee, *et al.* [6]:

$$K \;=\; \frac{1}{2}\left[\sum_{\alpha=1}^{N} X_\alpha K_\alpha + \left(\sum_{\alpha=1}^{N} X_\alpha/K_\alpha\right)^{-1}\right]. \tag{12}$$

We presently use the latter rule in COYOTE.

Calculation of the diffusional mass fluxes is a complicated task (for example, [7, 16,

19]. Many simulations simply use Fick's law,

$$\mathbf{J}_\alpha = -\rho D_\alpha \nabla(\rho_\alpha/\rho), \tag{13}$$

where ρ is the total density, and D_α is the species diffusivity. The original version of COYOTE used this approximation with the same value of D_α for all species, and this value was given as the kinematic viscosity of the mixture divided by a constant mixture Schmidt number. This simple model has the advantages that it is easy to program, computationally inexpensive, and the species mass fluxes properly add up to zero when summed over species. Experience suggests that it is adequate for turbulent flows (where molecular transport is overwhelmed by the turbulent eddy diffusion) and in some laminar cases (whenever high accuracy of the detailed chemical composition field is not critical). In other cases, such as the present study, differential diffusion effects are important and a more accurate model is required.

We use a more accurate model based on the Stefan-Maxwell equations [7]

$$\sum_\beta \left(X_\alpha X_\beta / D_{\alpha\beta}\right)\left(\mathbf{u}_\beta - \mathbf{u}_\alpha\right) = \mathbf{G}_\alpha \equiv \mathbf{d}_\alpha + \chi_\alpha \nabla \ln T \quad (\alpha = 1, \ldots N), \tag{14}$$

where N is the number of species in the mixture, $\mathbf{u}_\alpha$ is the velocity of species α, X_α is the mole fraction of species α, and $D_{\alpha\beta}$ is the binary diffusivity for the pair of species (α, β). The χ_α are related to the species thermal diffusion coefficients and will be discussed shortly. The diffusional mass fluxes are given by

$$\mathbf{J}_\alpha = \rho_\alpha(\mathbf{u}_\alpha - \mathbf{u}), \tag{15}$$

where $\mathbf{u}$ is the mass-weighted mixture velocity calculated from the momentum equation 2,

$$\rho\mathbf{u} = \sum_\alpha \rho_\alpha \mathbf{u}_\alpha. \tag{16}$$

The diffusional fluxes can be found by solving the coupled system 14 through 16 for each cell on each time step. This involves solving a linear system for each cell face on each cycle. The only real "trick" to doing this is to eliminate all rows of the matrix $X_\alpha X_\beta / D_{\alpha\beta}$ that are all zeroes before calling the linear system solver. The resulting matrix is still singular, so it is necessary to replace one row of the matrix with equation 16. We usually

select the row for the least abundant species. There can still sometimes be problems with the matrix being ill-conditioned, so in practice it occasionally is necessary also to eliminate rows for species with densities less than some cutoff value, which we normally take to be zero. With very low abundances, it is usually safe to assume the diffusional velocity is zero. It seems to help to solve for $X_\alpha \mathbf{u}_\alpha$ rather than for $\mathbf{u}_\alpha$, so the elements of βth row of the coefficient matrix are $X_\beta / D_{\alpha\beta}$.

We follow Hayashi and Hishida [12] in evaluation of the binary diffusion coefficients:

$$D_{\alpha\beta} = \frac{3}{16}\left(\frac{2k_{\rm B}^3}{\pi m_{\rm H}}\right)^{1/2} \frac{\left[T^3\left(\frac{M_\alpha+M_\beta}{M_\alpha M_\beta}\right)\right]^{1/2}}{P\sigma_{\alpha\beta}^2\Omega_{\rm D}} f_{\rm D} = 1.8829\times 10^3 \frac{\left[T^3\left(\frac{M_\alpha+M_\beta}{M_\alpha M_\beta}\right)\right]^{1/2}}{P\sigma_{\alpha\beta}^2\Omega_{\rm D}}, \qquad (17)$$

where P is the total pressure of the mixture and $f_{\rm D}$ is a correction factor in the range $1.0 \le f_{\rm D} \le 1.1$. We take $f_{\rm D} = 1.0$, and the numerical factor in the right equality assumes cgs units except for $\sigma_{\alpha\beta}$, which is in Ångstroms. We also use

$$\sigma_{\alpha\beta} = 0.5\,(\sigma_\alpha + \sigma_\beta), \qquad (18)$$

$$\Omega_{\rm D} = (T/T_{e\alpha\beta})^{-0.145} + (T/T_{e\alpha\beta} + 0.5)^{-2}, \qquad (19)$$

and

$$T_{e\alpha\beta} = (T_{e\alpha}T_{e\beta})^{1/2}. \qquad (20)$$

It is common practice to ignore the thermal diffusion terms and set $\chi_\alpha = D_\alpha^T = 0$. Not only are thermal diffusion effects generally small, there are practical difficulties associated with obtaining the required values of χ_α. There is a shortage of experimental data, and the traditional theory is so complex as to hinder its application by the nonspecialist. However, Ramshaw has developed an approximate simplified theory [20, 21] that has been incorporated into COYOTE. This model is valid only for ideal gases, and we shall specialize it to the one-temperature case. The first step is to estimate the collision cross section between molecules of types α and β as

$$\zeta^{\alpha\beta} = 0.25\pi(\sigma_\alpha + \sigma_\beta)^2. \qquad (21)$$

We define

$$\gamma_{\alpha\beta} = \frac{m_{\rm H}}{2k_{\rm B}T}\frac{M_\alpha M_\beta}{M_\alpha + M_\beta}. \qquad (22)$$

With these two parameters we calculate the collision time

$$\tau_\alpha = \frac{1}{2}\left[\sum_{\beta=1}^{N} \frac{n_\beta \zeta^{\alpha\beta}}{(\pi\,\gamma_{\alpha\beta})^{1/2}}\right]^{-1}, \tag{23}$$

where n_β is the number density of species β. Next we calculate

$$\mathcal{B}_{\alpha\beta} = -\frac{RTPX_\alpha X_\beta M_\alpha \tau_\beta}{2D_{\alpha\beta}M_\beta(M_\alpha + M_\beta)}, \tag{24}$$

which are in turn used to calculate the χ_α using the left equality of

$$\chi_\alpha = P^{-1}\sum_{\beta=1}^{N}(\mathcal{B}_{\beta\alpha} - \mathcal{B}_{\alpha\beta}) = \sum_{\beta=1}^{N}\frac{X_\alpha X_\beta}{D_{\alpha\beta}}\left(\frac{D_\alpha^T}{\rho_\alpha} - \frac{D_\beta^T}{\rho_\beta}\right). \tag{25}$$

The χ_α are used in the Stefan-Maxwell equations 14, which in turn are used with equation 15 to calculate the diffusion fluxes. The second equality in equation 25 is a linear system that can be solved for the D_α^T for use in evaluating the Dufour term in the energy flux. This system is singular, and one equation must be replaced by the constraint

$$\sum_\alpha D_\alpha^T = 0. \tag{26}$$

3 Numerical Simulations

In this section we present a simulation of the helium jet experiment discussed by Jacobs [1]. We elected to run this problem in three separate pieces. First, we ran a series of one-dimensional shocks to find the post-shock conditions that produce a planar shock with the correct propagation speed, which is Mach 1.093-1.095 in the experiments. Second, we ran a simulation of a cross section of the jet without a shock so molecular diffusion would produce the correct transition region between the air and the jet material. The PLIF image plane is 3.81 cm above the jet orifice, so a Lagrangian fluid element has a significant amount of time for diffusion to occur during advection between the orifice and the image plane. Third, we combined the shock wave and the "aged" jet cross section to produce simulations of the interaction between the two.

Unfortunately, little in the way of quantitative comparisons can be done with this experiment. First, the results are a time sequence of PLIF images taken from several different runs of the experiment. Second, no length scales or position data are given with the images.

Third, the precise experimental conditions are not given. For example, all we know about the shock is its Mach number. We have to guess at everything else. Air is not a simple substance [22]; it can have a mole fraction of water varying between zero and eight percent at standard pressure and temperature. No temperature, pressure, or humidity were given for the air in the shock tube. Also, there was neither information on how the sound speed used to get the Mach number was estimated, nor information on the shock velocity or jump conditions. The composition of the jet mixture also is poorly known as we are given only an imprecise description of how the helium-biacetyl mixture was prepared. Since the baroclinic torques that drive the deformation of the jet depend on the density and pressure gradients, the present simulations can be at best semi-quantitative.

3.1 The Planar Shock Wave in Air

The nominal shock Mach number in these experiments is 1.093-1.095. Rather than beginning with the analytic shock jump conditions, we made a separate run of the planar shock without the jet to fine-tune the jump conditions to get a numerical Mach 1.095 shock without significant oscillations near the shock front. This insures that the numerical shock wave is consistent with the gas physics used in the code. Table 2 is the COYOTE input file for the final combined calculation. The initial conditions in the unshocked air are set by region 1 input, and the post-shock air is set by region 3 input. Note that we treat air as a five-component mixture rather than as a single material. The species index numbers are the same as in Table 1, and the calculation is performed in the laboratory frame.

3.2 Diffusion of the Helium Jet

We estimate from the experimental flow conditions that the helium jet requires approximately 29 ms to advect a Lagrangian fluid element from the jet orifice to the PLIF image plane. During this time, molecular transport will smear out the composition gradient at the interface between the jet and the ambient air. In their simulations, Greenough and Jacobs [2] assume that the helium mole fraction on the cylinder axis has been reduced to 80% of its original value by this time, and that the concentration profile is a Gaussian with the diameter at half the maximum concentration of 0.666 cm. Rather than use this assumption, we made

a preliminary run without a shock wave and let the cylinder of helium spiked with biacetyl "age" for 29 ms. Since we did not have the enthalpy table or transport coefficients for biacetyl, we used those for isohexane. This should be quite accurate since the molecular weights are the same and the biacetyl molecule has the same basic molecular structure as one of the hexane isomers (2,3-dimethylbutane). The COYOTE isohexane transport coefficients agree with those for biacetyl given by Jacobs.

The mole and mass fractions of He and biacetyl after 29 ms with no flow are shown in figures 1-4. The left boundary is a plane of symmetry. Figure 1 shows the helium mole fraction. At $t = 0$, there is a discontinuity between the round helium jet and the surrounding air, and this discontinuity coincides with the fifth contour (labelled f) in figure 1. Initially, the helium mole fraction is 0.99474. In figure 1, the central mole fraction has been reduced to 0.84744. Figure 2 shows the helium mass fraction, which has decreased from 0.89773 to 0.40684. Notice that the mole fraction contours are significantly more spread out than those for the mass fraction. Figures 3 and 4 show the mole and mass fractions for biacetyl, respectively. The central values have gone from 0.00526 and 0.10227 to 0.00911 and 0.09389. Note that the central mole fraction has increased even though the mass fraction has decreased. This is due to the intermediate molecular weight of the air molecules that replace the helium. Also, differential diffusion causes the helium contours to be far more spread out than the biacetyl contours. Since kinetic theory predicts that transport coefficients scale approximately as $M_\alpha^{-1/2}$, this is the correct behavior of the detailed molecular transport model. It shows that biacetyl is not necessarily a good marker for the helium if there is sufficient time for diffusion to be important.

The PLIF signal strength is proportional to the density of biacetyl molecules, so the appropriate quantity to plot for comparison to the experimental images is the species density. This is shown for both He and biacetyl in figures 5 and 6. Once again, we see a substantial difference between the two plots. Biacetyl is not a reliable marker of either initial jet material or its helium component.

3.3 The Shocked Helium Jet

The shock wave described in Section 3.1 and the diffused jet cross section described in Section 3.2 were combined to create the initial condition for the shocked jet simulation. This initial condition was created by taking the "aged" no-flow solution at 29 ms and "cutting out" a large patch of zones containing the diffused jet and placing it in a grid in which the shock wave had been initialized at the bottom of the grid. The time evolution was then begun and followed in the usual fashion.

Figure 7 shows the contours of total density in the intitial condition. The shock wave appears at the bottom of the figure as a single straight line. The important point of this figure is that the density is monotonically increasing away from the center of the jet, even though the differential diffusion enhances the concentration of the heavy biacetyl there. The direction of this gradient is important because it determines the sign of the baroclinic torques produced by the shock wave, and hence the direction of rotation when the helium cylinder collapses into a pair of line vortices.

Figures 3b through 3f of reference [1] should be compared to my figures 8 through 12. The shock wave passes the jet at 30 μs in the calculation, so all of my problem times must be offset by that much to agree with the experimental times. My figures 8 through 10 are in excellent agreement with Jacobs' figures 3b through 3d. Comparison of my figures 11 and 12 to Jacobs' 3e and 3f show the simulation lagging behind a little in the rate of development of the roll-up. Also, the thin layer of biacetyl on the centerline is becoming thicker than in the experiment. Finer resolution should improve this situation. The simulation was terminated at this point since the jet is about to exit the grid.

Figure 13 shows the density of helium at the same time as figure 12. We see a significant amount of helium in the region between the centerline and the vortex. This is not seen in the biacetyl plot or in the experiment. This is further evidence that the biacetyl is not a good marker for helium in this experiment.

4 Conclusions

We have performed a DNS of a jet of helium-biacetyl mixture interacting with a low-Mach number shock wave. This is a preliminary study that demonstrates several things.

1. We used direct solution of the Stefan-Maxwell equations for the mass diffusion fluxes within a multidimensional finite difference computational fluid dynamics program based on the multicomponent Navier-Stokes equations. The full algorithm has been used in test problems with as many as 21 species and is quite practical for much more complex mixtures than used in the present study.

2. Molecular transport, in particular differential diffusion, is important in this problem. Specifically, the helium and biacetyl separate significantly during the time the jet material takes to advect from the jet orifice to the PLIF image plane. This means that biacetyl is a poor marker for the helium.

3. The jet undergoes sufficient molecular diffusion as the fluid travels from the jet orifice to the image plane that it makes no sense to model it with a sharp interface between the two gases.

4. Even though the jet material is advected most of the length of the mesh, the amount of numerical diffusion is quite small.

5. Future work should include redoing these simulations in a reference frame in which the shocked ambient medium is stationary. This would not only eliminate almost all numerical diffusion, it would allow the use of a shorter grid, thereby making the calculation more efficient. We should also try a finer grid.

6. We should also simulate the jet in the plane containing its axis of symmetry in order to incorporate buoyancy effects into the timing of the fluid arrival at the image plane. This will be shorter than 29 ms. We expect slightly less molecular diffusion, but this could partially be compensated by a thinning of the jet due to the buoyant acceleration. However, we do not expect a dramatic change in the final results.

5 Acknowledgments

This work was performed under the auspices of the U. S. Department of Energy by University of California Lawrence Livermore National Laboratory under contract number W-7405-ENG-48.

References

[1] J. W. Jacobs, "The dynamics of shock accelerated light and heavy gas cylinders," Phys. Fluids A **5**, 2239 (1993).

[2] J. A. Greenough and J. W. Jacobs, "A numerical study of shock-acceleration of a diffuse helium cylinder," in Proceedings of the Fifth International Workshop on Compressible Turbulent Mixing, ed. R. Young, J. Glimm, and B. Boston, World Scientific, Singapore, 1996, pp. 338-345.

[3] J. W. Jacobs, "Shock-induced mixing of a light-gas cylinder," J. Fluid Mech. **234**, 629 (1992).

[4] L. D. Cloutman, "COYOTE: A Computer Program for 2-D Reactive Flow Simulations," Lawrence Livermore National Laboratory report UCRL-ID-103611, 1990.

[5] L. D. Cloutman, "On the role of mass diffusion and fluid dynamics in the dissipation of chunk mix," Lawrence Livermore National Laboratory report UCRL-ID-133412, 1999.

[6] R. J. Kee, G. Dixon-Lewis, J. Warnatz, M. E. Coltrin, and J. A. Miller, "A Fortran Computer Code Package for the Evaluation of Gas-Phase Multicomponent Transport Properties," Sandia National Laboratories report SAND86-8246, 1986; reprinted 1995.

[7] J. O. Hirschfelder, C. F. Curtiss, and R. B. Bird, *Molecular Theory of Gases and Liquids* (Wiley, New York, 1964).

[8] D. R. Stull and H. Prophet, "JANAF Thermochemical Tables, 2nd ed.," U. S. Department of Commerce/National Bureau of Standards report NSRDS-NBS 37, 1971.

[9] M. W. Chase, J. L. Curnutt, A. T. Hu, H. Prophet, A. N. Syverud, and L. C. Walker, "JANAF Thermochemical Table, 1974 Supplement," J. Phys. Chem. Ref. Data **3**, 311 (1974).

[10] M. W. Chase, Jr., C. A. Davies, J. R. Downey, Jr., D. J. Frurip, M. A. McDonald, and A. N. Syverud, "JANAF Thermochemical Tables, Third Edition, Parts I and II," Supplement No. 1, J. Phys. Chem. Ref. Data **14** (1985).

[11] L. D. Cloutman, "A Selected Library of Transport Coefficients for Combustion and Plasma Physics Applications," Lawrence Livermore National Laboratory report UCRL-ID-139893, 2000.

[12] A. K. Hayashi and M. Hishida, "Numerical Study on Pulsed Jet Combustion," in *Fourth International Symposium on Computational Fluid Dynamics, Vol. III*, University of California at Davis (1991), pp. 19-24.

[13] F. M. White, *Viscous Fluid Flow* (McGraw-Hill, New York, 1974).

[14] L. Monchick and E. A. Mason, "Transport properties of polar gases," J. Chem. Phys. **35**, 1676 (1961).

[15] C. R. Wilke, "A Viscosity Equation for Gas Mixtures," J. Chem. Phys. **18**, 517 (1950).

[16] R. B. Bird, W. E. Stewart, and E. N. Lightfoot, *Transport Phenomena* (Wiley, New York, 1960).

[17] J. H. Ferziger and H. G. Kaper, *Mathematical Theory of Transport Processes in Gases* (North-Holland, Amsterdam, 1972).

[18] S. Mathur, P. K. Tondon, and S. C. Saxena, "Thermal conductivity of binary, ternary, and quaternary mixtures of rare gases," Mol. Phys. **12**, 569 (1967).

[19] S. Chapman and T. G. Cowling, *The Mathematical Theory of Non-Uniform Gases* (Cambridge University Press, London, 1952).

[20] J. D. Ramshaw, "Hydrodynamic theory of multicomponent diffusion and thermal diffusion in multitemperature gas mixtures," J. Non-Equilib. Thermodyn. **18**, 121 (1993).

[21] J. D. Ramshaw, "Simple approximation for thermal diffusion in gas mixtures," J. Non-Equilib. Thermodyn. **21**, 99 (1996).

[22] L. D. Cloutman, "What is Air? A Standard Model For Combustion Simulations," Lawrence Livermore National Laboratory report UCRL-ID-144664, 2001.

[23] J. K. Dukowicz and J. D. Ramshaw, "Tensor viscosity method for convection in numerical fluid dynamics," *J. Comput. Phys.*, **32**, 71 (1979).

Table 2.

COYOTE Input File

Base Case Input (cgs units)

```
&coydat
ncyc=0, nclast=5000, ncfilm=5000,
tclast=3.0d-05, printv=3.d-06, lpr=0, idebug=0,
xlam0=0.2, xlamfl=0.,
npatch=1,
nchlim=0,
alf_1=1.1d-02, alf_0=0.8d+00,
Afram=5.d+00, Bfram=1.d+00,
Cfram=3.d+00, Dfram=1.d+00,
Efram=3.d+00, Ffram=1.d+00,
nsubzx=1,
izxtype(1)=1, subzxl(1)=0.00, subzxr(1)=2., noxz(1)=126,
 subdxl(1)=0.1,
nsubzy=1,
izytype(1)=1, subzyl(1)=0., subzyr(1)=5.2d+00, noyz(1)=326,
  subdyl(2)=0.1,
alpha=0.02, beta=0.98,
dtmax=-2.d-08, delt=5.d-09, autot=1., cyl=0.,
kr=1, kl=1, kb=6, kt=3, epsp=1.e-08, airmu=0., rhood=1.,
ndtits=40, dtrat=1.005, gx=0., gy=0.,
patmt=1.013d+06, patmr=1.013d+06, patml=1.013d+06, patmb=1.25251d+06,
keps=0, algsgs=0., atke=0.117, dtke=1.4, charl=0., charlf=0.,
cbuoy=0., lrect=1, cbuoyad=0.d+00, ynumol=0., swrl=0.,
low_intens=1, Ret_crit=5.d+00, cntrgrd=0.d+00,
charlg=3.75, cbscat=0.,
scmol=0.7, scsgs=0.7, prmol=0.7, prsgs=0.7,
tcut=700., tcute=1200., itptype=2,
lwr=0, twr=300., kpoutt=1,
lwt=0, lwl=0, lwb=0,
tvflag=1.,
nregn=3, ispecl=0,
is(1)=1, ie(1)=127, js(1)=1, je(1)=327,
 treg(1)=295.,
 rhoreg(1,1)=0.d+00,
 rhoreg(1,2)=2.769649094d-04,
 rhoreg(1,3)=9.033253488d-04,
 rhoreg(1,4)=5.453366356d-07,
 rhoreg(1,5)=5.152377715d-08,
 rhoreg(1,6)=1.534859876d-05,
 rhoreg(1,7)=0.d+00,
 rhoreg(1,8)=0.d+00,
 ureg(1)=0., vreg(1)=0.d+05, omgreg(1)=0.,
 tkereg(1)=0.d+06, epsreg(1)=0.,
is(2)=1, ie(2)=40, js(2)=5, je(2)=174,
 treg(2)=295.,
 rhoreg(2,1)=1.8732958d-05,
 rhoreg(2,2)=0.d-04,
```

```
 rhoreg(2,3)=0.d-04,
 rhoreg(2,4)=0.d-07,
 rhoreg(2,5)=0.d-08,
 rhoreg(2,6)=0.d-05,
 rhoreg(2,7)=1.644417662d-04,
 rhoreg(2,8)=0.d+00,
 ureg(2)=0., vreg(2)=0.d+04, omgreg(2)=0.,
 tkereg(2)=0.d+06, epsreg(2)=0.,
 xcen(2)=0.d+00, ycen(2)=1.d+00, radius(2)=0.397,
is(3)=1, ie(3)=127, js(3)=1, je(3)=7,
 treg(3)=3.13462d+02,
 rhoreg(3,1)=0.0d-05,
 rhoreg(3,2)=2.769649094d-04,
 rhoreg(3,3)=9.033253488d-04,
 rhoreg(3,4)=5.453366356d-07,
 rhoreg(3,5)=5.152377715d-08,
 rhoreg(3,6)=1.534859876d-05,
 rhoreg(3,7)=0.d+00,
 rhoreg(3,8)=0.d+00,
 denmul(3)=1.1636043d+00,
 ureg(3)=0., vreg(3)=5.30565d+03, omgreg(3)=0.,
 tkereg(3)=0.d+06, epsreg(3)=0.,
nobs=0,
nsp=8,
eosform(1)=2., eosform(2)=2.,
eosform(3)=2., eosform(4)=2.,
eosform(5)=2., eosform(6)=2.,
eosform(7)=2., eosform(8)=2.,
&end
&tranco
  mixvis=2,
  jtdiff=3, jtco=11, jtco2=4, jth2o=5,
  jdradv=1, jdrflg=2, jdrsm=1, jdrdbg=0,
&end
&chemin
 nre=0, nrk=0, ntaps=0, printt=1.05, kwikeq=2, jchem=1,
&end

Jacobs' experiment - shocked cylinder of He
10/30/01

species list:
 1  C4H14 (foo biacetyl)
 2  O2
 3  N2
 4  CO2
 5  H2O
 6  A
 7  He
 8  SF6
```

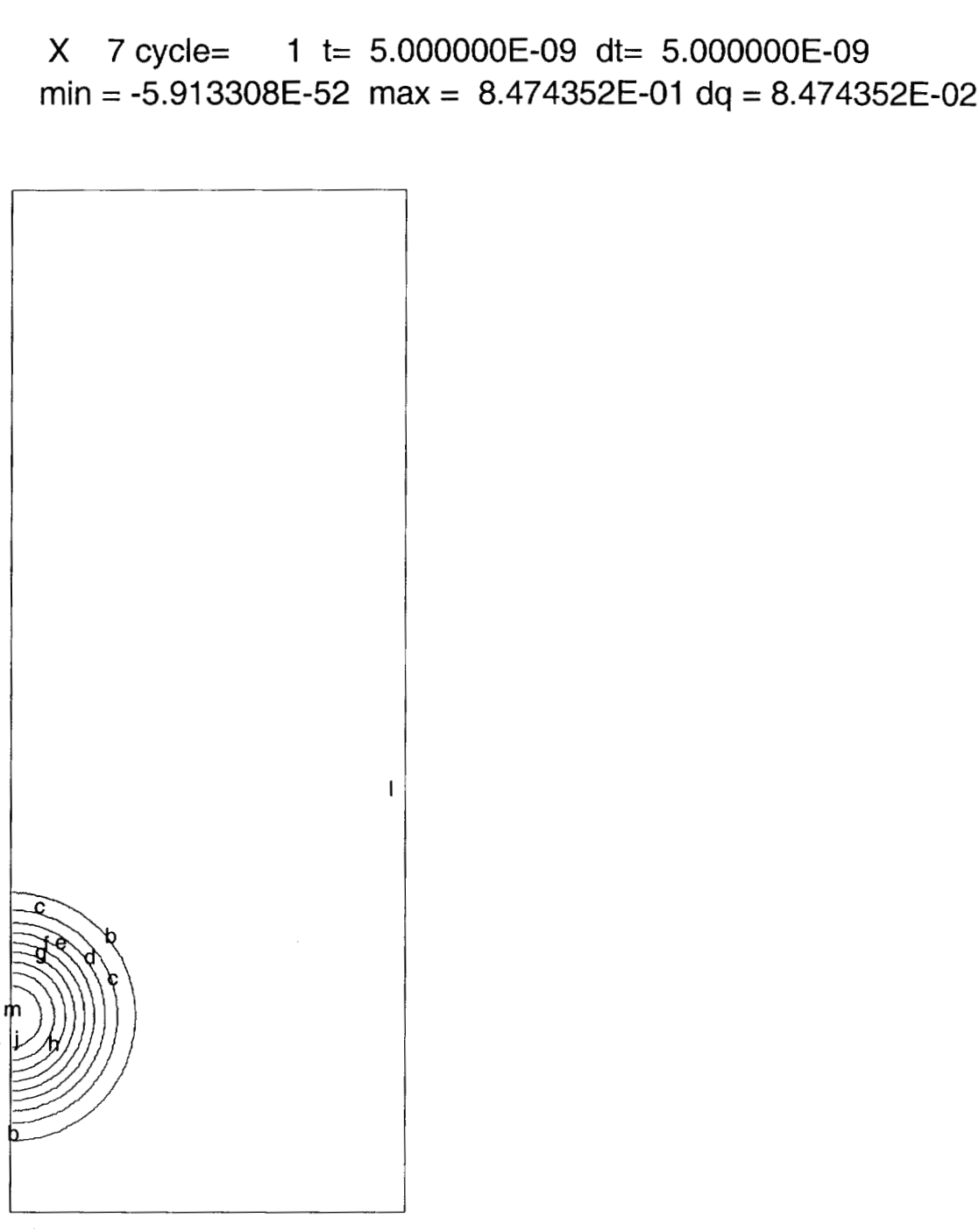

Figure 1: Helium mole fraction after the 29 ms "aging" process in which diffusion is allowed to act in the absence of fluid flow. The problem time has been reset to zero. The nine contours (labeled b through j) are separated by 10% of the difference between the minimum (l) and maximum (m) values in the grid.

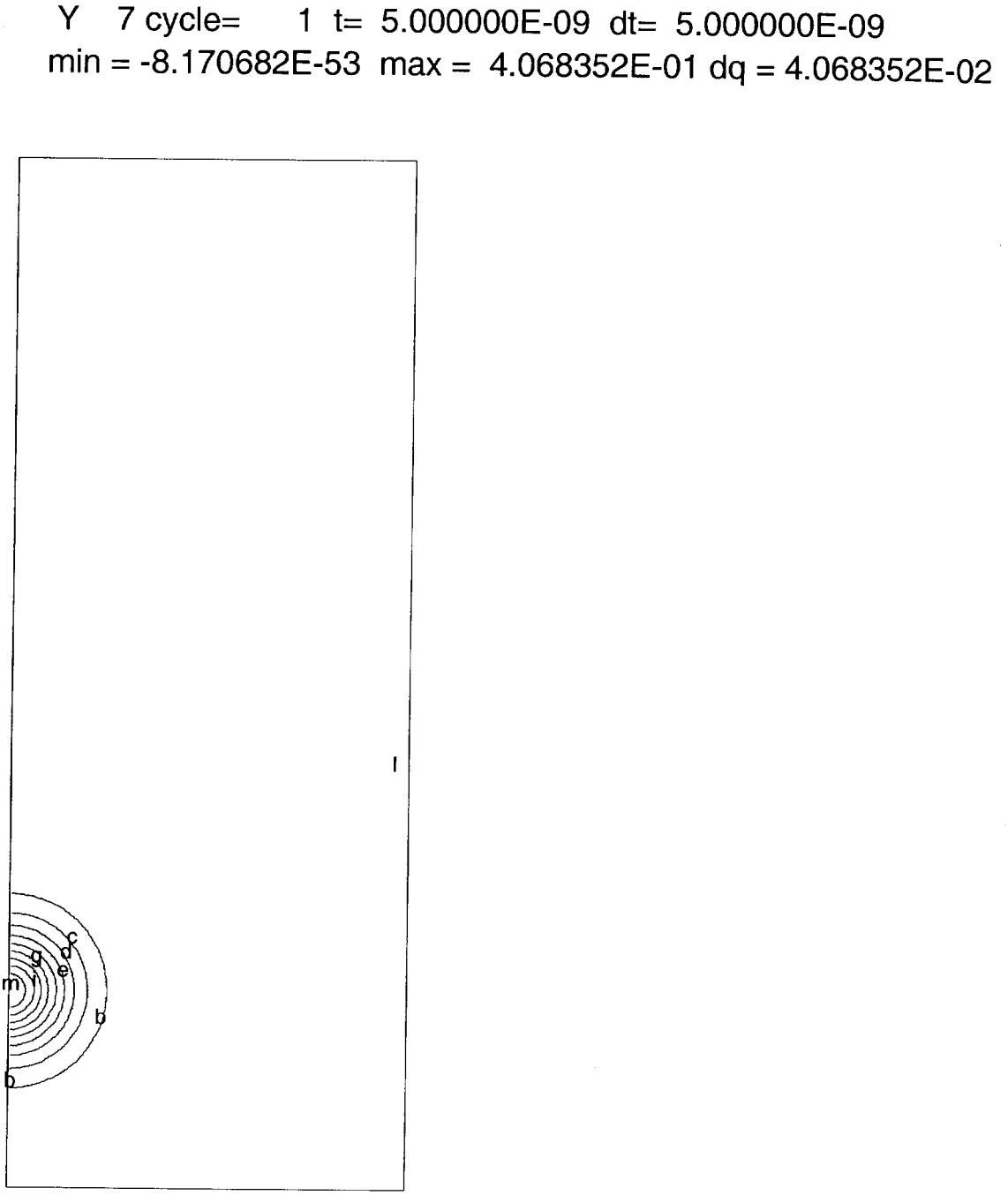

Figure 2: Helium mass fraction after "aging."

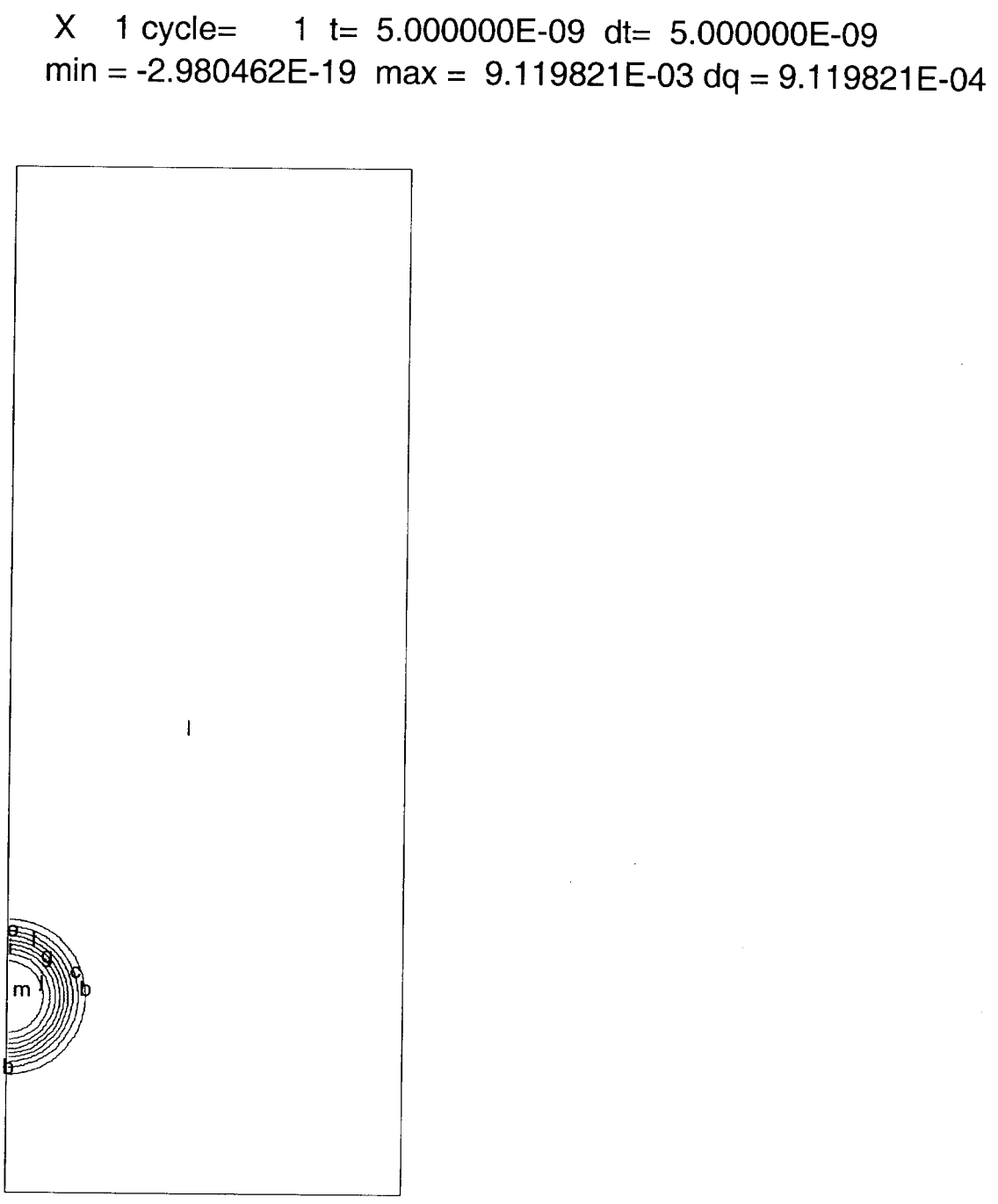

Figure 3: Biacetyl mole fraction after "aging."

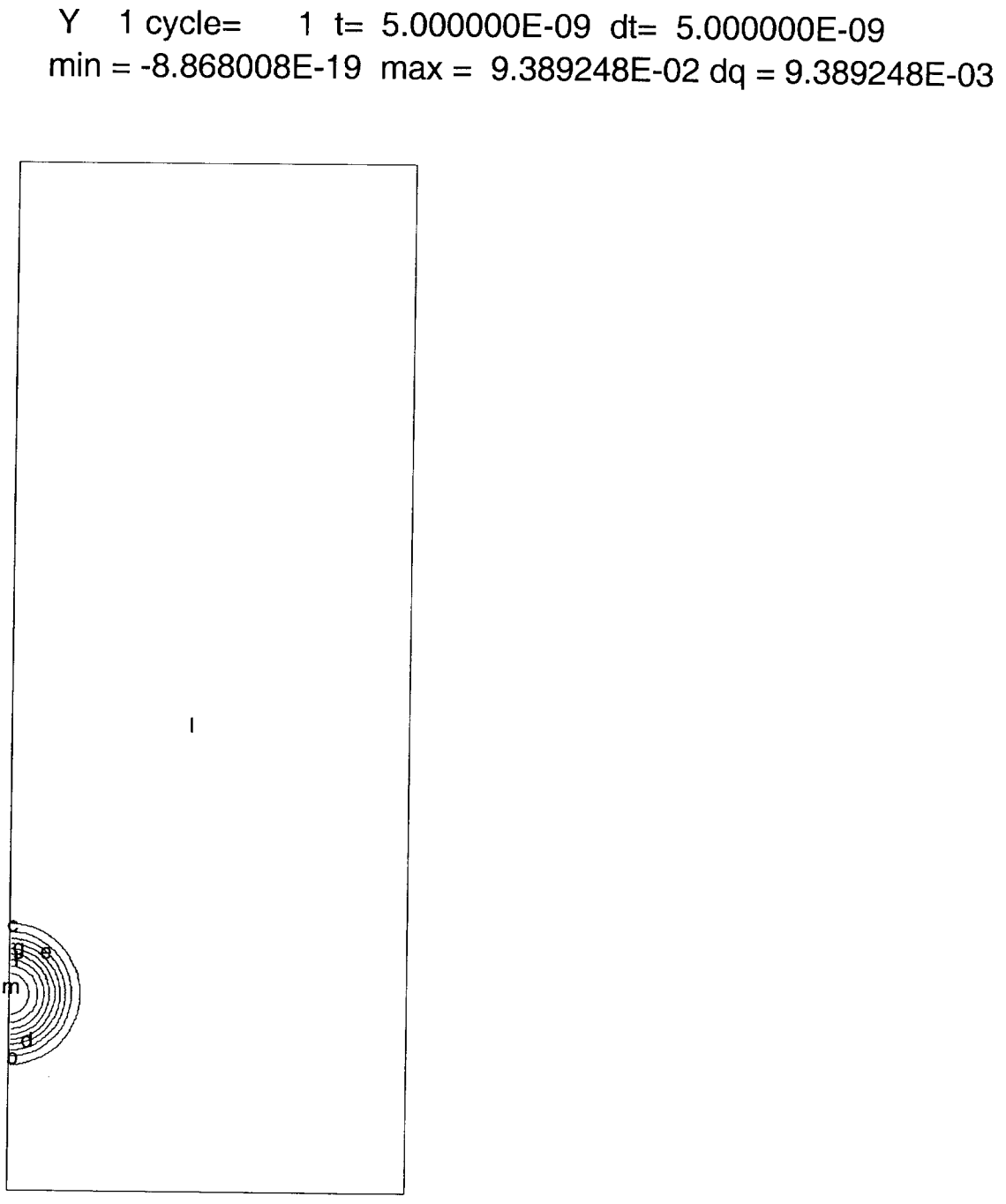

Figure 4: Biacetyl mass fraction after "aging."

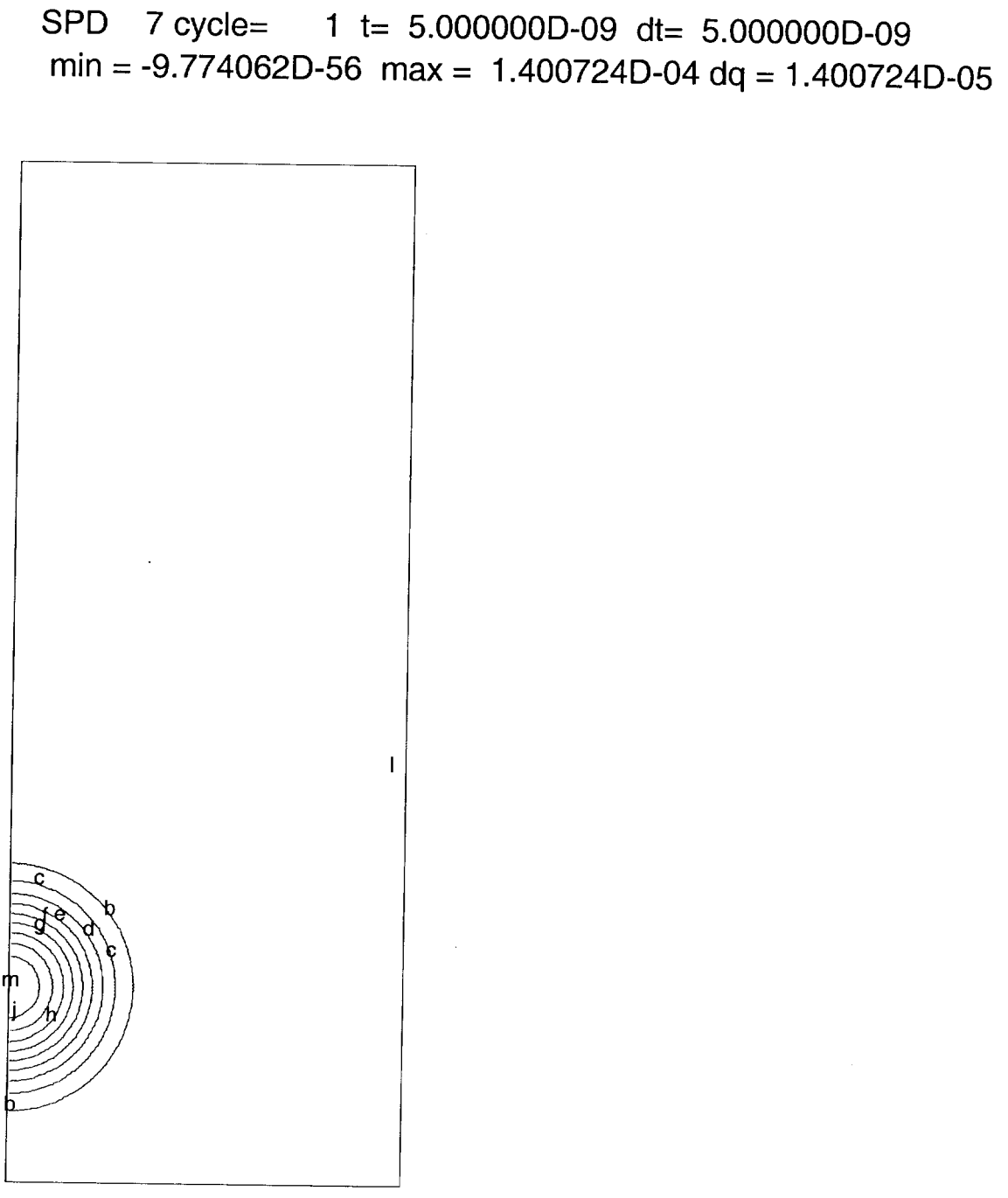

Figure 5: Helium species density after "aging."

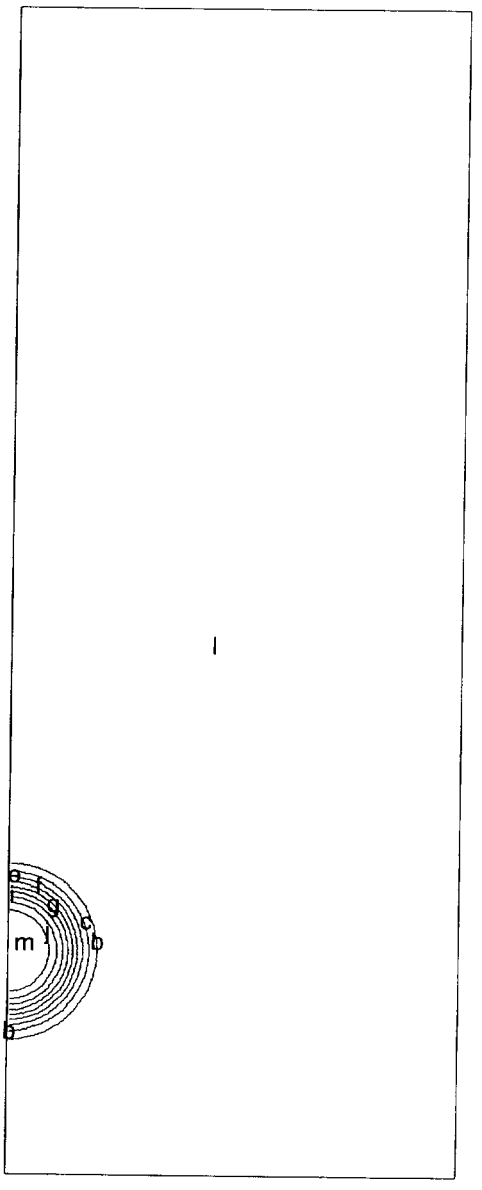

Figure 6: Biacetyl species density after "aging."

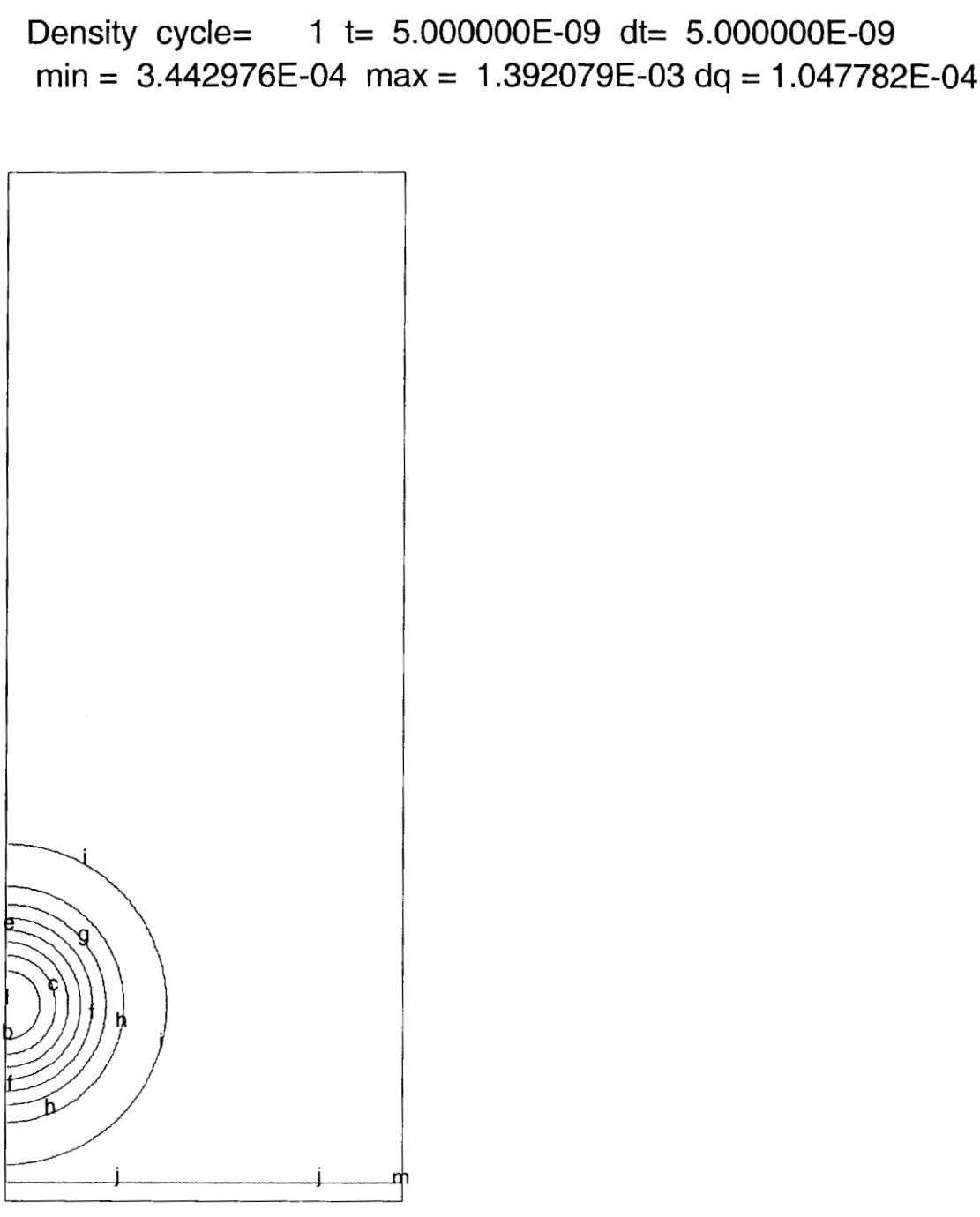

Figure 7: Total mass density contours after "aging." The straight line at the bottom is the impinging shock wave moving upward.

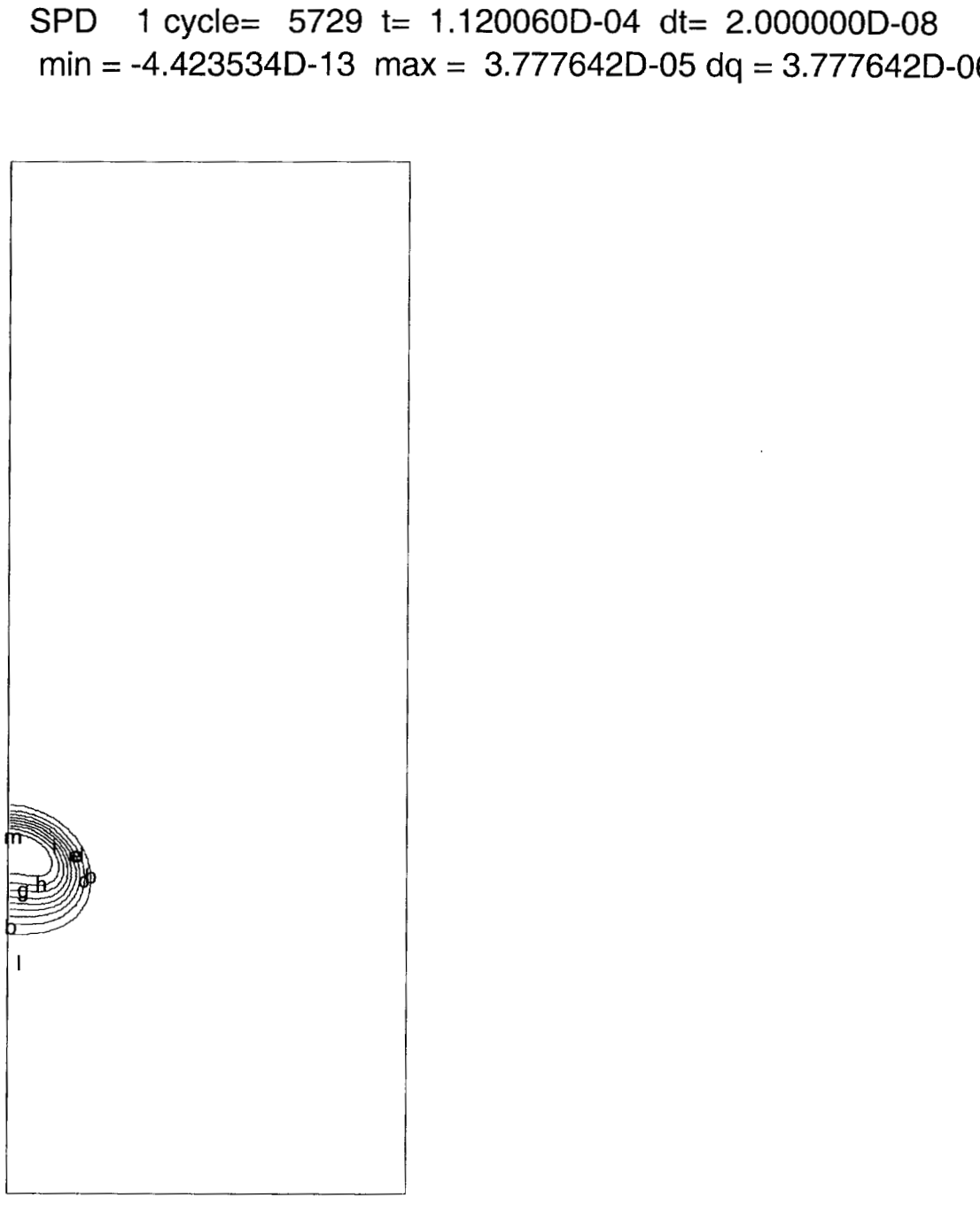

Figure 8: Biacetyl species density at 82 μs after shock passage.

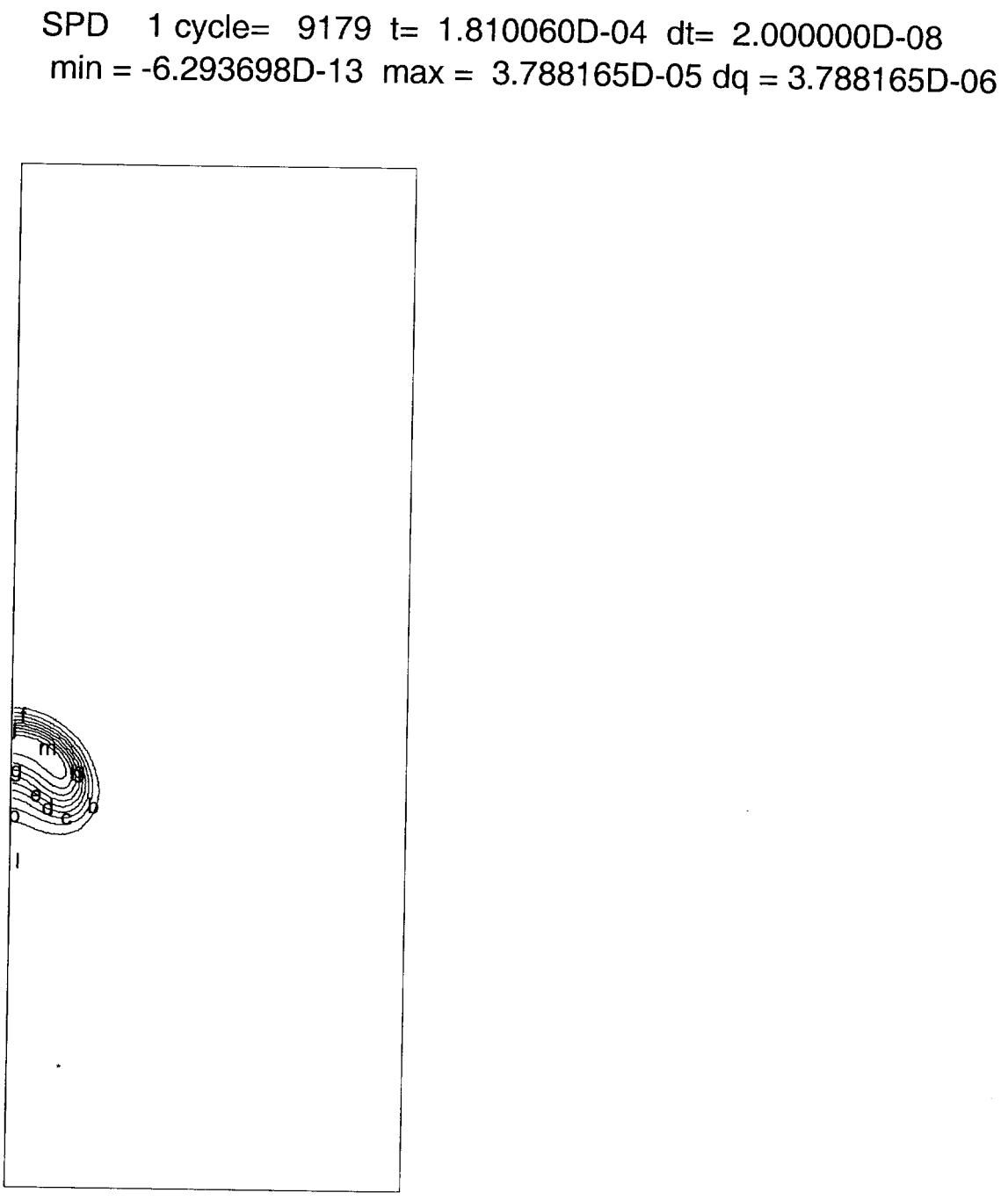

Figure 9: Biacetyl species density at 151 μs after shock passage.

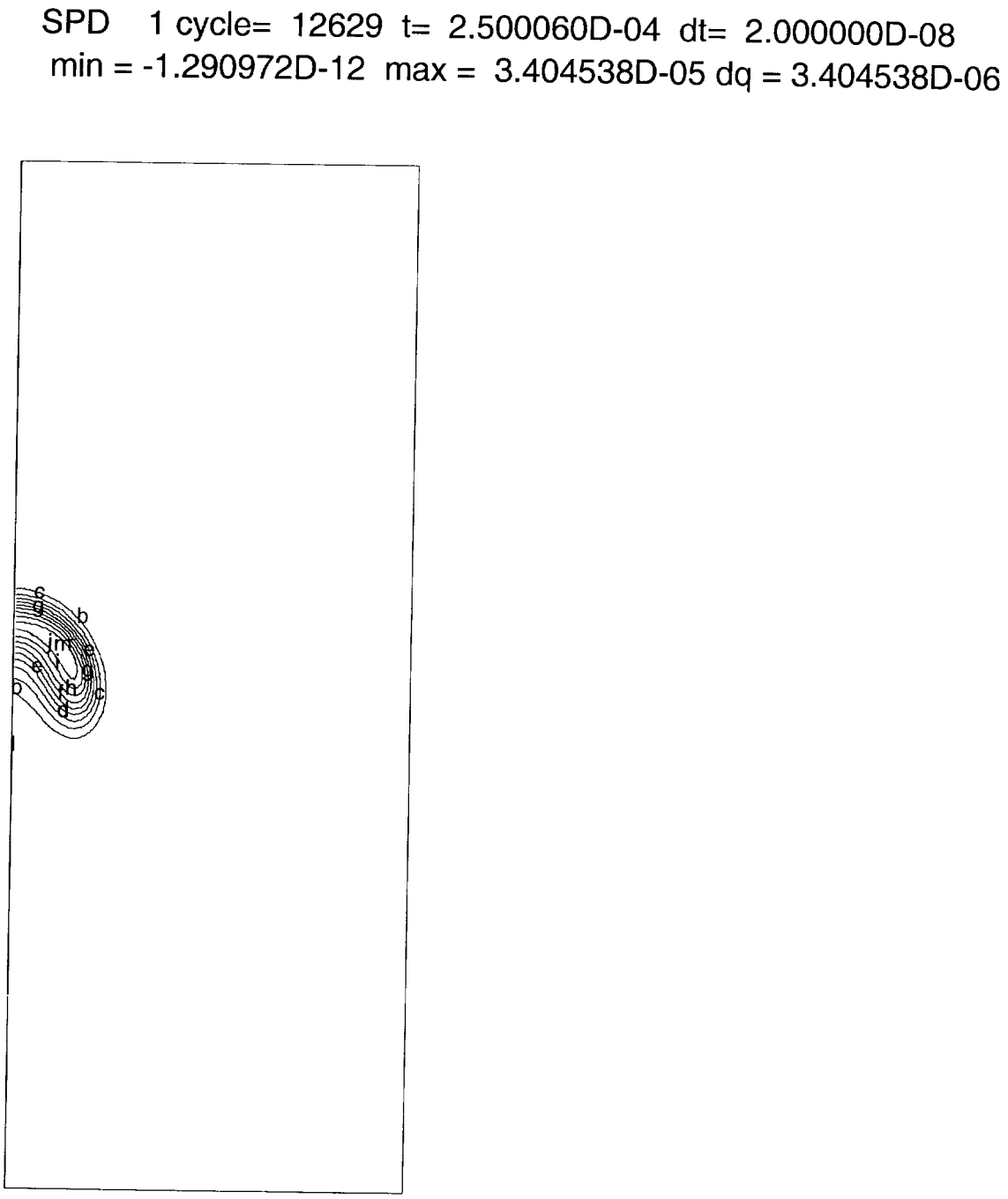

Figure 10: Biacetyl species density at 220 μs after shock passage.

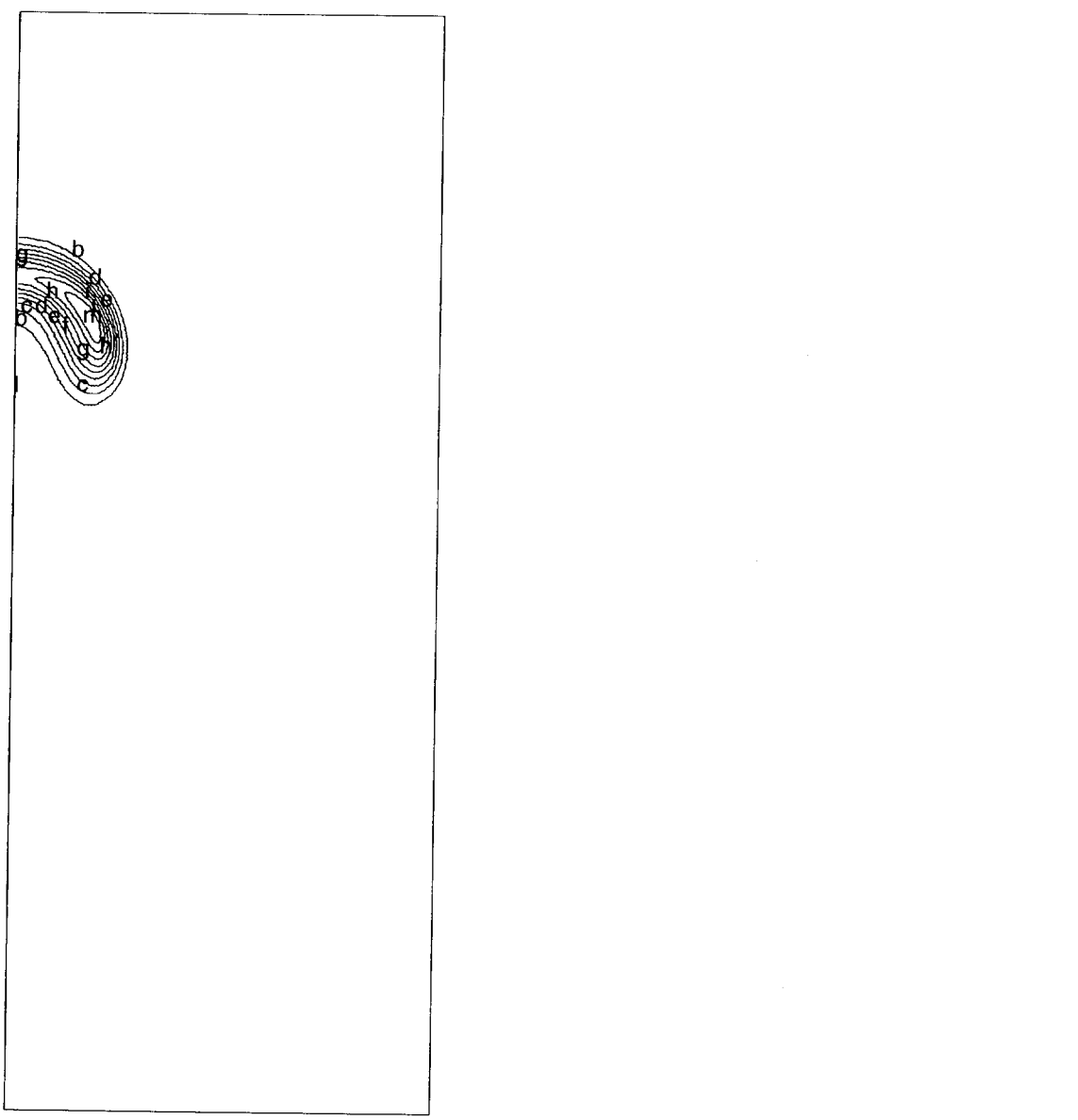

Figure 11: Biacetyl species density at 319 μs after shock passage.

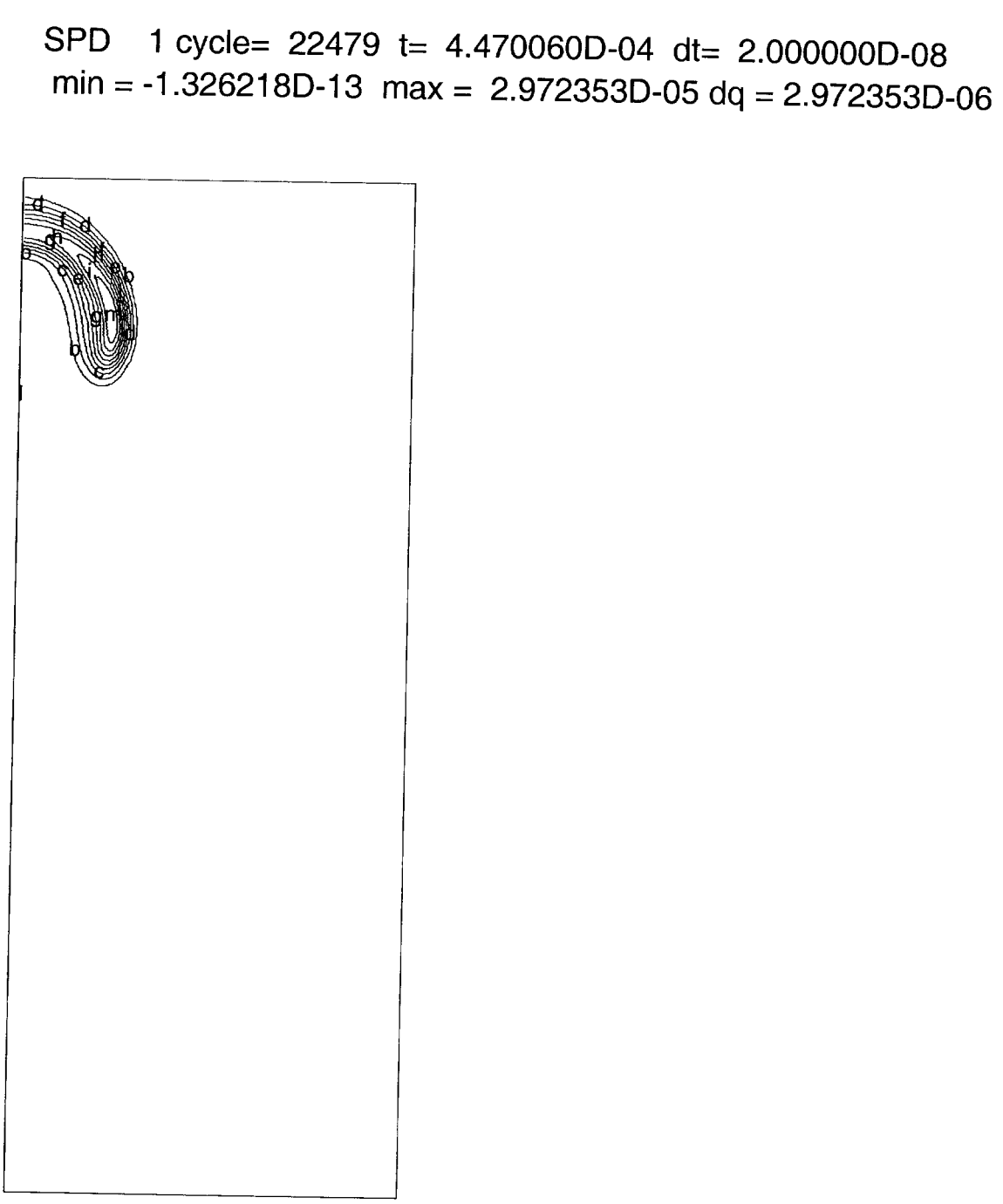

Figure 12: Biacetyl species density at 417 μs after shock passage.

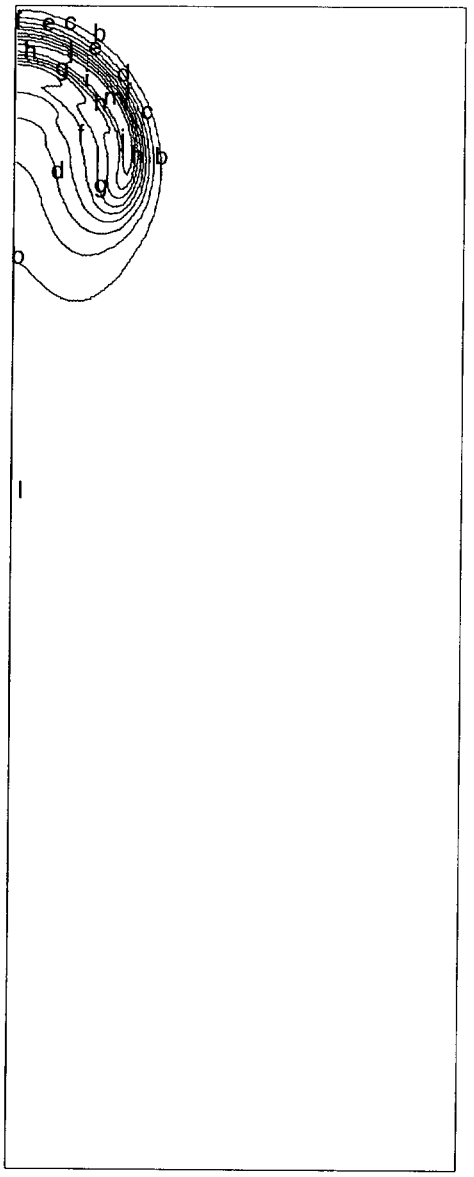

Figure 13: Helium species density at 417 μs after shock passage.